Journal of Materials Chemistry C

Accepted Manuscript

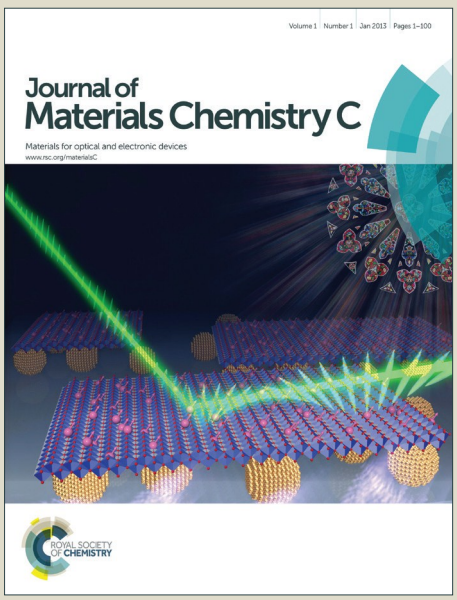

ROYAL SOCIETY OF CHEMISTRY

www.rsc.org/materialsC

Journal Name

ARTICLE

Ag@Au Hexagonal Nanorings: Synthesis, Mechanism Analysis and Structure-dependent Optical Characteristics

Received 00th January 20xx,
Accepted 00th January 20xx

DOI: 10.1039/x0xx00000x

www.rsc.org/

Wei Lai,[a] Jun Zhou,*[a] Zhenhong Jia,[b] Lucia Petti[c] and Pasquale Mormile[c]

Well-shaped Ag@Au hexagonal nanorings (Ag@Au HNRs) were successfully synthesized with the assistance of Ag hexagonal nanoplates as structure-directing templates in a galvanic replacement route, and their optical characteristics were studied in detail. During the synthetic process, the morphology of the Ag@Au HNRs was found to be strongly depended on the dosage of $HAuCl_4$ added into the template solution. Both the experimental and calculated absorption spectra showed that the red-shift of localized surface plasmon resonance (LSPR) peaks of the Ag@Au HNRs obeyed a modified Lorentz function with increasing the dosage of $HAuCl_4$ solution, which was also explained by the plasmon hybridization of the Ag@Au HNRs. Moreover, the surface-enhanced Raman scattering (SERS) characteristic of Ag@Au HNRs were investigated by using 4-mercaptobenzoic acid (4MBA) as Raman reporter molecule. And the as-prepared Ag@Au HNRs have excellent SERS performances with an enhancement factor ~ 10^6, especially for the Ag@Au HNR prepared at 160 μl $HAuCl_4$ solution due to its strongest plasmons electric-field enhancement. It reveals that the as-synthesized Ag@Au HNRs possess a great potential for the application in ultrasensitive biosensor.

Introduction

Noble metal nanostructures have drawn considerable interests for their unique optical properties and intriguing applications in the chemical and biosensing fields.[1-4] For instance, the localized surface plasmon resonance (LSPR) characteristics of noble metal nanostructures can be tailored in the visible and near infrared (NIR) spectral region which is suitable to detect the biological tissues by using an incident radiation in the "window of optical transparency".[5] The surface-enhanced Raman scattering (SERS), as the most famous consequence of plasmonic coupling effect,[6] is a powerful fingerprint technique for detecting of the molecules adsorbed on the surface of noble metal nanostructures with a remarkably improved sensitivity.[7] And it is well known that the SERS performances were mainly subjected to the electromagnetic enhancement originating from the LSPR which is intensively dependent on the shape and size of noble metal nanostructures.[8] Especially, the LSPR characteristics of the hollow bimetallic nanostructures are not only sensitive to their morphology and size but also their composition.[9-13] Concretely, the LSPR peaks of the hollow bimetallic nanostructures can be easily tuned across the visible and NIR spectrum region with changing the of the morphology of nanostructure such as the size of the hollow interior and the metallic component ratio. And the hollow bimetallic nanostructures displayed stronger SERS enhancement than that of the solid bimetallic nanoparticles with a same dimension owing to the multipole plasmon coupling existed at the hollow nanostructures.[14] It is obvious that the optical properties of the hollow bimetallic nanostructures are different from that of their solid counterparts. Therefore, it has great significance to design novel bimetallic hollow nanostructures with a well-controlled morphology and compositions for achieving structure-dependent LSPR characteristic and SERS efficiency.

Recently, many template-assisted methods have been developed to synthesize various hollow bimetallic nanostructures, including Kirkendall effect, chemical etching, galvanic replacement and template-mediated approach.[15] In principle, all of these synthesized methods exploit solid nanoparticles as sacrificial templates that are dissolved or transformed to generate hollow nanostructures based on the reduction potential of the metal.[16] For example, Puntes and his co-workers reported a synthetic strategy of producing several hollow bimetallic nanostructures *via* the simultaneous or sequential actions of galvanic replacement and Kirkendall effect.[17] Yamauchi's group developed a facile route to prepare Pt-Pd bimetallic nanocages with dentritic shells by using selective chemical etching.[18] Bao and colleagues put forward a novel method to achieve large-scale preparation of Pt-Co nanoshells based on the template-mediated approach.[19] And most of these methods are involved the usage of a extra reducing agent, such as ascorbic acid (AA), which resulted in the formation of hollow bimetallic alloy nanostructures.[20] However, to our knowledge, without the help of extra reducing agent, the galvanic replacement route aimed at the production of a hollow

[a] *Institute of Photonics, Faculty of Science, Ningbo University, Ningbo 315211, China. Tel: +86-574-87600794; Fax: +86-574-87600744; E-mail: zhoujun@nbu.edu.cn*
[b] *School of Information Science and Engineering, Xinjiang University, Urumqi 830046, China.*
[c] *Institute of Cybernetics "E. Caianiello" of CNR, Via Campi Flegrei 34, 80072 Pozzuoli, Ital.*

† Electronic Supplementary Information (ESI) available: Size effect of the gold nanosphere, relationship of wall thickness and the dosage of $HAuCl_4$ solution, and plasmon hybridization.

bimetallic nanostructure is rare. Therefore, it is meaningful to prepare a hollow bimetallic nanostructure with the controllable LSPR and SERS characteristics through a galvanic replacement approach.

In this paper, we present a facile galvanic replacement route for synthesizing Ag@Au core-shell hexagonal nanorings (Ag@Au HNRs) based on the structure-directing templates of Ag hexagonal nanoplates (Ag HNPs).[21] In the synthetic process, the morphologies and internal cavity sizes of the Ag@Au HNRs clearly demonstrate the evolution with the increasing of the dosage of $HAuCl_4$ solution. And, the formation mechanism of Ag@Au HNRs has been tentatively explained by analysing the spectroscopic and crystallographic characteristics. Meanwhile, the experimental UV-Vis absorption spectra show that LSPR bands of the Ag@Au HNRs exhibited an interesting relationship of Lorentz function's dependence on the dosages of $HAuCl_4$ solution, which is also theoretically simulated by finite element method (FEM). Lastly, the SERS performances of Ag@Au HNRs were investigated by using 4-mercaptobenzoic acid (4MBA) as a Raman reporter molecule in detail and display a strong dependence on the dosages of $HAuCl_4$ solution, that is, the structure-dependent SERS characteristics.

Experimental

Chemicals

Silver nitrate ($AgNO_3$), hexadecyl trimethyl ammonium bromide (CTAB) and hydrogen tetrachloroaurate (III) trihydrate ($HAuCl_4 \cdot 3H_2O$) were purchased from Sigma-Aldrich. Trisodium citrate and ascorbic acid (AA) were purchased from Tianjin Bodi Chemical Co., Ltd. (Tianjin, China). Sodium borohydride ($NaBH_4$) was purchased from Sinopharm Chemical Reagent Co., Ltd. (Shanghai, China). Sodium hydroxide (NaOH) was purchased from Zhejiang Zhongxing Chemical Reagent Co., Ltd. (Zhejiang, China). 4-mercaptobenzoic acid (4MBA) was obtained from J&K Scientific Co., Ltd. Deionized water (Millipore Milli-Q grade) with resistivity of 18.2 $M\Omega \cdot ml^{-1}$ was used to prepare all solutions. All chemicals were the analytic grade and used as received.

Synthesis of Ag HNPs

Ag HNPs as the sacrificial template were synthesized by using the seed-mediated growth approach with the assistance of CTAB. Typically, the seed solution (20 ml) was prepared by adding 0.6 ml freshly prepared ice-cold 0.01M $NaBH_4$ solution into the mixture solution containing 0.25 mM $AgNO_3$ and 0.25 mM trisodium citrate under stirring vigorously for 30 s. And the colour of the seed solution appeared light yellow rapidly. Subsequently, the growth solution containing 20 ml of 0.05 M CTAB, 0.6 ml of 0.01 M $AgNO_3$, 1.5 ml of 0.01M AA and 0.6 ml of 1 M NaOH, was prepared. Then, 0.6 ml of the seed solution was added into the growth solution, and the reaction solution was gently agitated for 2 min. Lastly, Ag HNPs solution was obtained and its colour changed into turquoise blue within 2 min.

Synthesis of Ag@Au HNRs and 4MBA-tagged Ag@Au HNRs

The as-prepared Ag HNPs solution was divided into eight aliquots to be used for preparing the sample solutions of Ag@Au HNRs. To synthesize Ag@Au HNRs, different dosages (0-600 μl) of 4.65×10^{-4} M $HAuCl_4$ were added into the Ag HNPs solutions accompanying with vigorous stirring. After several minutes, the colour of sample solutions, depending on the added dosage of $HAuCl_4$ solution, were observed from mauve to purple. To remove the excess CTAB and other impurities, the sample solutions were centrifuged consecutively two times at 8,000 rpm for 30 min and then dispersed into 2 ml of deionized water for further use, respectively.

The 4MBA-tagged Ag@Au HNRs were prepared by adding 20 μl of 1 mM 4MBA ethanol solutions into the as-purified Ag@Au HNRs solutions under stirring and agitated for 10 h. Next, the unbound 4MBA molecules in the solutions were removed by centrifuging at 8,000 rpm for 30 min, and then, the 4MBA-tagged Ag@Au HNRs settled to the bottom were dispersed in 2 ml of deionized water.

Instruments

Absorption spectra were measured by using an UV-Vis spectrometer (TU-1901, Pgeneral). Transmission electron microscope (TEM) images, dark-field scanning TEM (STEM) images, high-resolution transmission electron microscope (HRTEM) images, selective area electron diffraction (SAED) pattern, energy-dispersive X-ray spectroscopy (EDS) and STEM EDS mapping were obtained using a TEM (JEM-2100F, JEOL) operated at accelerating voltage of 200 kV. The X-ray diffraction (XRD) pattern was measured by using an X-ray diffractometer (D8 DISCOVER, Bruker). SERS signals were measured by using a Raman spectrometer (BWS415, B&W Tek Inc.) which is equipped with a semiconductor laser (785-nm, 499.95 mW), the dispersed grating of 1200 $lines \cdot mm^{-1}$ and the charge-coupled device (CCD) (2048×2048 pixels) detector. All the analyses were performed at room temperature.

Results and discussion

Morphology and growth mechanism of Ag HNPs and Ag@Au HNRs

The Ag@Au HNRs were prepared by using the Ag HNPs as initial sacrificial templates through a one-spot galvanic replacement route. The typical morphologies of Ag HNPs and Ag@Au HNRs prepared at different dosages of $HAuCl_4$ solutions are displayed in Fig. 1. As shown in Fig. 1, the Ag HNPs composed of {111} facets have an average size of 38 ± 4 nm, and the Ag@Au HNRs exhibit a variety of average sizes from 38 ± 4 to 62 ± 5 nm accompanying with increasing of the dosage of $HAuCl_4$ solution from 80 to 600 μl. After thoroughly completing of the galvanic replacement reaction, the wall thickness of Ag@Au HNRs synthesized at 600 μl $HAuCl_4$ solution was 4±0.4 nm, which is only one eighth of the dimension of the origin Ag HNPs by comparing Fig. 1(a) with Fig. 1(h).

For visually understanding the formation of Ag@Au HNRs, Fig. 2 outlines the chemical process transforming of Ag HNPs into Ag@Au HNRs. Initially, the Ag atoms were reduced from the Ag^+ ions by AA and deposited on the surfaces of Ag nanoparticles to form the hexagonal plate nanostructure because the CTAB monolayers have selectively adsorbed on the {111} crystal planes for inducing anisotropic growth of different planes.[21] Then, the galvanic replacement reaction between Ag HNPs and $HAuCl_4$ resulted in the dissolution of Ag atoms in the interior of Ag HNPs by

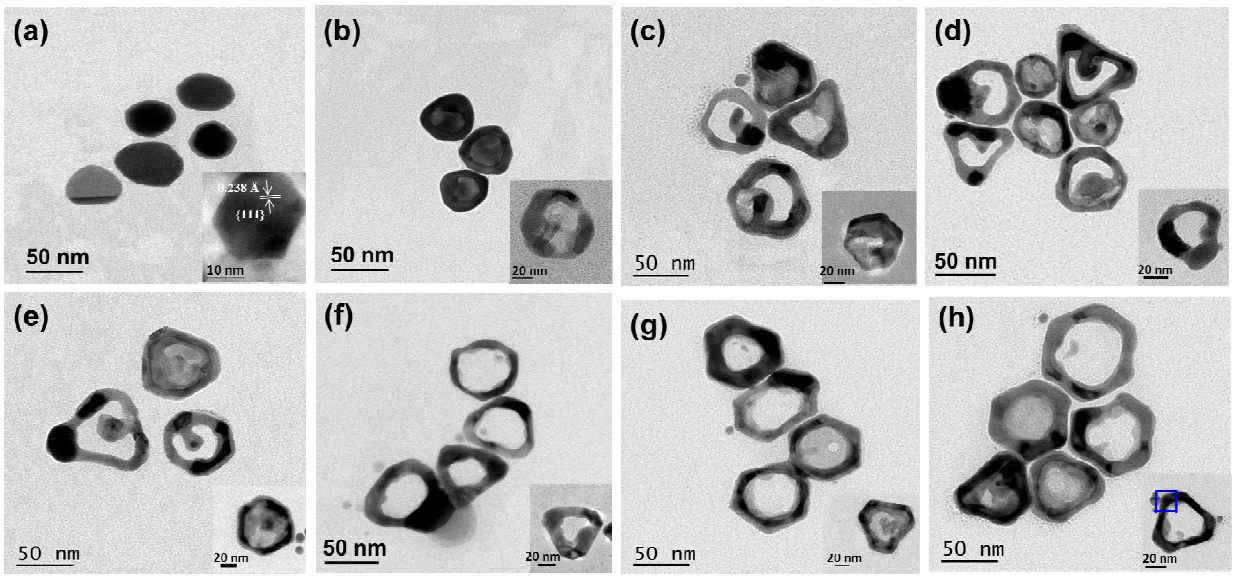

Fig. 1 TEM images of Ag HNPs (a) and Ag@Au HNRs obtained at different dosages of $HAuCl_4$ solution, (b) 80 µl, (c) 120 µl, (d) 160 µl, (e) 200 µl, (f) 300 µl, (g) 400 µl and (h) 600 µl. The insets show the TEM images of the individual Ag HNP (a) and Ag@Au HNR (b-h) at a higher magnification. The blue square area in (h) was used to carry out the HRTEM image of Ag@Au HNR in Fig. 3(b) later.

the migration of electrons, and the reduction of $AuCl_4^-$ ions generate Au atoms and led to the formation of a gold shell for lowering the energetic cost.[22] And as shown in Fig. 1(b)-1(h), along with the disappearance of the internal Ag atoms, the external gold shell continually shrank with increasing of the dosages of $HAuCl_4$ solution to minimize the surface energy until the generation of Ag@Au HNRs. In addition, it is worth noting that the Ag^+ and Cl^- ions in the reaction solution also played an important role to promote the formation of Ag@Au HNRs by driving down the reduction potential of Ag^+/Ag redox pair. Meanwhile, the indiscerptible AgCl were generated and settled to the bottom of the container as white solid precipitate at room temperature, which has made an advantage to obtain pure sample owing to the absence of AgCl.[23]

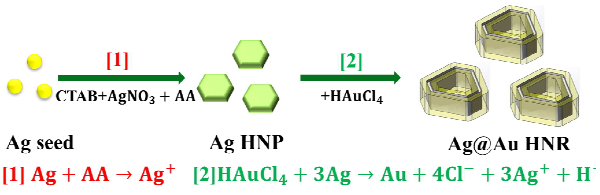

Fig. 2 Schematic of the growth mechanism of Ag@Au HNRs

Furthermore, to providing insights into the growth mechanism, the crystallography and the geometry of Ag@Au HNRs was investigated by analysing the SAED pattern, HRTEM image, XRD pattern and EDS mapping of Ag@Au HNRs. As shown in Fig. 3(a), the SAED patterns demonstrate that the individual Ag@Au HNRs is a poly-crystalline comprised of the main crystal facets {111} and the formally forbidden 1/3{422}. And the appearance of formally forbidden 1/3{422} reflections is suggested a centre of inversion symmetry with respect to the [111] axis consistent only with <111> poly-crystalline with irregular twins.[24] Concurrently, the HRTEM image of Ag@Au HNR (Fig. 3(b)) was collected from the blue square area in inset of Fig. 1(h) and displays relatively strong fringes with a spacing of 2.38 Å and 2.5 Å which are respectively corresponded to the {111} and formally forbidden 1/3{422} reflections in the SAED pattern, according to the JCPDS file 04-0784. And there is no an clear interface of Au and Ag due to the Kirkendall effect and a small lattice mismatch (0.17%) in the Ag@Au system.[25, 26] It is well-known that the free energies of various crystal faces decrease in the order of $\gamma_{\{110\}} > \gamma_{\{100\}} > \gamma_{\{111\}}$ for the face-centred cubic (fcc) metal crystal, such as silver and gold,[27] so the final shape and geometry of nanostructure is determined by the distribution of exposed crystallographic facets which promotes the selective growth in certain crystallographic directions.[28] Among these three low-index crystallographic facets, the {111} facets have a close-packed arrangement of atoms and are the most thermodynamically favoured facets.[31] And, according to the stoichiometric relationship, the galvanic replacement reaction against the two {111} planes of silver plate (thickness < 10 nm) could not generate enough gold atoms to construct two continuous {111} planes for gold shell,[4] which resulted in the formation of the hexagonal rings by using Ag HNPs as sacrificial template in our experiment. Also, minor reconstructions occur in the galvanic replacement reaction to eliminate the embowed edges into straight edges, which is benefit for preparing the hexagonal nanorings with regular morphology. These results are consistent with the XRD pattern of Ag@Au HNRs shown in Fig. 3(c). Comparing the experimental XRD pattern of Ag@Au HNRs with that of pure crystal of Au and Ag (JCPDS 04-0784 and 04-0783, respectively), it is clear that the diffraction peaks of as-prepared Ag@Au HNRs are matched well with that of the Au and Ag crystal, which indirectly indicated that the Ag@Au HNRs are mainly consisted of Ag and Au crystal. To further confirm the nanostructure, the elemental mapping of the Ag@Au HNRs has been measured. In Fig. 3(d), the STEM

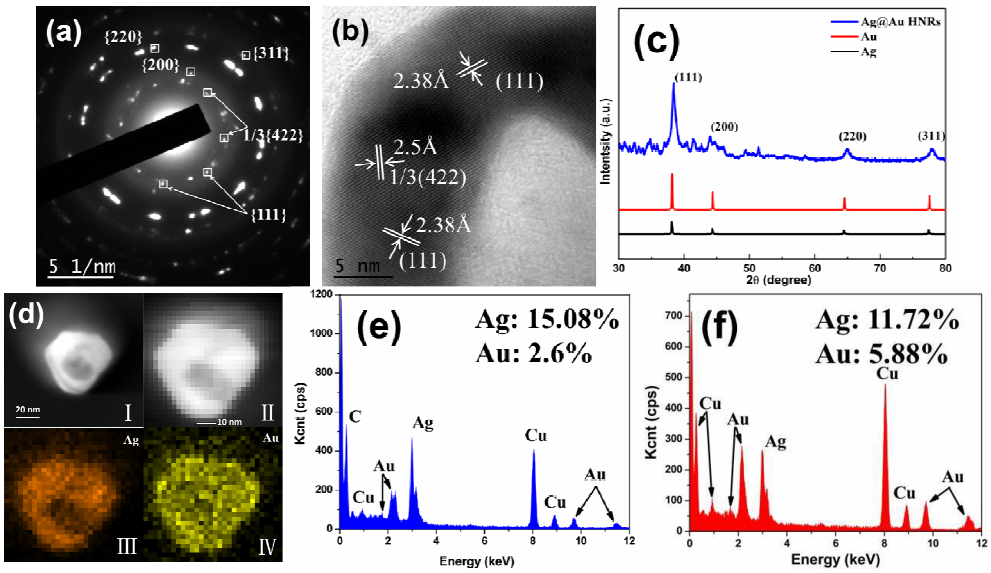

Fig. 3 (a) SAED pattern, (b) HRTEM image and (c) XRD pattern of Ag@Au HNRs prepared at 600μl $HAuCl_4$; (d) Images of dark-field TEM (I), STEM (II), EDS mapping of Ag (III) and Au (IV) of of Ag@Au HNR; EDS of Ag@Au HNRs obtained at different dosages of $HAuCl_4$ solution: (e) 160 μl and (f) 600 μl.

EDS mapping of the same hexagonal nanoring region defined clearly the spatial distributions of Au and Ag in individual nanoring that is consistent with the expected Ag ring @Au shell structure. In addition, Fig. 3(e) and (f) clearly show that the as-prepared hexagonal nanorings are only made of Ag and Au atoms and the atomic ratio of Au/Ag has a significant increase with increasing of the dosage of $HAuCl_4$ solution from 160 μl to 600 μl.

LSPR property of Ag HNPs and Ag@Au HNRs

In our experiments, the galvanic replacement reaction between $HAuCl_4$ and Ag HNPs was followed by using UV-Vis spectroscopic method. Fig. 4(a) provides the UV-Vis absorption spectra of the Ag@Au HNRs prepared at different dosages of $HAuCl_4$ solution, and the inset also exhibits the colour of resulted solutions ranged from light yellow to modena accompanied with the increased dosages of $HAuCl_4$ solution. As shown in Fig. 4(a), the three plasmon resonance peaks of Ag HNPs located respectively at 345, 417, and 550 nm, which corresponded to the case without $HAuCl_4$ solution. However, the plasmon resonance peaks of the Ag@Au HNRs red-shifted with the increasing of dosages of $HAuCl_4$ solution, from initial 417 and 550 nm to final 532 and 737 nm, respectively, and 345 nm peak almost disappeared. Fig. 4(b) gives the experimental dependence of peak positions on the dosages of $HAuCl_4$ solution, and the fitted curves can be illustrated very well by a modified Lorentz function[32] expressed as follow:

$$P = P_0 + \frac{2A}{\pi}\frac{V_0}{4(V+V_c)^2 + V_0^2} \qquad (1)$$

where the parameters of y_0, A, ω and x_c are all the constant. For curve 1, P_0 = 290.79818 nm, $A = 5.2534\times10^5$ nm·μl, V_0 = 724.73114 μl and V_c = 323.41351 μl; and for curve 2, P_0 = 538.35887 nm, $A = -3.3748\times10^4$ nm·μl, V_0 = 176.62336 μl and V_c = -9.76335 μl. It is interesting why the red-shift of LSPR peaks of Ag@Au HNRs dependent on the dosages of $HAuCl_4$ solutions obeys the form of a modified Lorentz function. As a comparison, the calculated absorption spectra of gold nanosphere with different radii and the relationship of LSPR peak to the volume of gold nanosphere are

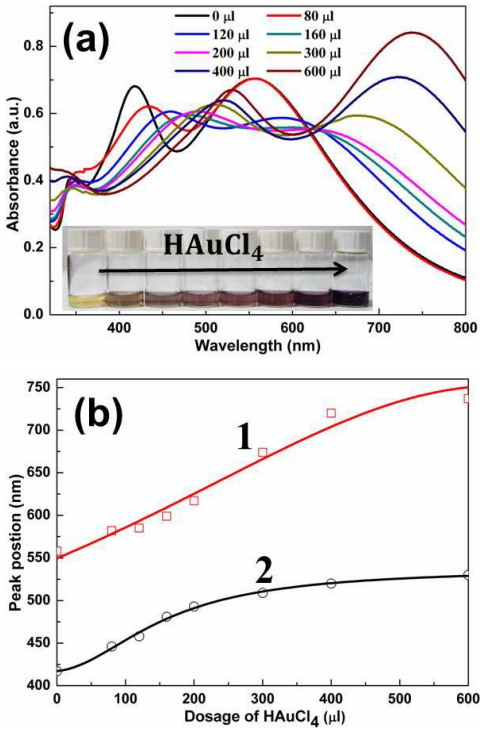

Fig. 4 (a) The UV-Vis absorption spectra of Ag HNPs and Ag@Au HNRs prepared at various dosages of 4.65×10^{-4} M $HAuCl_4$ (0-600 μl), the inset is the solution colour at different dosages of $HAuCl_4$ solution, (b) plot of the dependence of peak position (P) on the dosage of $HAuCl_4$ solution (V) for the 550-nm (curve 1) and 417-nm (curve 2) peaks.

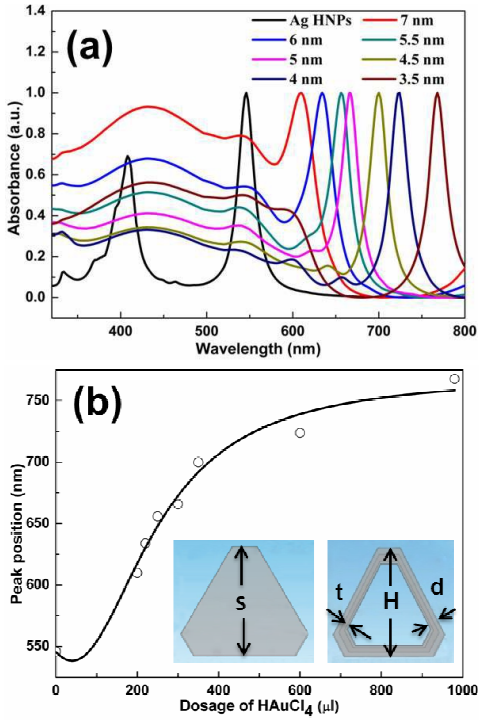

Fig. 5 (a) The absorption spectra of Ag HNPs and Ag@Au HNRs with different wall thicknesses; (b) the dipole plasmon LSPR peaks (P) *vs* the dosage of $HAuCl_4$ solution (V), and the black curve is their fitted curve. The left inset is Ag HNP model and right is Ag@Au HNRs model. In our calculations, S = 40 nm, H = 52 nm, d is the wall thickness of the Ag@Au HNR, and t is the wall thickness of Ag ring which is half of d.

shown in Fig. S1(a) and (b), respectively. By coincidence, the fitted curve in Fig. S1(b) is also a Lorentz curve. Thus, similarly to the result of gold nanosphere, it could be concluded that the red-shifts of LSPR peaks in our experiments come from the synergy of the components, the shape and the size of Ag@Au HNRs.

To further investigate the structure-dependent LSPR characteristics of the as-prepared Ag@Au HNRs, the optical absorption spectra of the Ag HNPs and Ag@Au HNRs were numerically simulated by using the FEM software (COMSOL Multiphysics 4.3). In our calculations, the dimensions of the Ag HNP and Ag@Au HNR models were extracted from the TEM images in Fig. 1, as shown in the insets of Fig. 5. The incident light was polarized along the horizontal direction and normally irradiated on the models. In Fig. 5(a), three main LSPR peaks of Ag HNPs are located at 345, 408 and 546 nm, respectively, which is considerably consistent with the experimental results (Fig. 4(a)). As the formation of Ag@Au HNRs, the calculated absorption spectra exhibit a few of LSPR peaks which are assigned to the plasmon resonant coupling of dipole, quadrupole, and multipole modes, respectively,[29] and the dipole plasmon resonant peaks located at longer wavelength red-shift from 546 to 768 nm with decreasing of the wall thickness. Actually, as well known, such red-shifts of the absorption bands were caused by the hybridization of the simultaneously excited plasmons on the outer and inner surface of individual metallic ring. Typically, the two plasmons will interact to produce a high-energy mode and a low-energy mode which correspond, respectively, to the anti-symmetric coupling (anti-bonding) and the symmetric coupling (bonding) between the cavity and the ring plasmons.[30] In addition, as the thickness of the ring becomes thinner, the interaction of the two plasmons becomes stronger and results in a larger energy separation between the high-energy mode and the low-energy mode (Fig. S3, ESI†). As a result, a distinct red-shift of the LSPR band occurs. In fact, as described in section 3.1, the wall thickness of Ag@Au HNRs was dependent on the dosage of $HAuCl_4$ solution. As shown in Fig. S2, the wall thickness d is the function of the dosage V, which follows Eq. (S2). Based on this relationship, the dosage-dependent positions of dipole LSPR peaks were plotted in Fig. 5(b) and can be fitted into a Lorentz curve by Eq. (1), here, P_0 = -3957.18992 nm, A = 7.36288×10^7 nm·μl, V_0 = 9874.44592 μl and V_c = 1152.81349 μl. Obviously, the red-shift of LSPR peaks follows the same trend of the experimental results, however, their difference was arose from the neglected interactions among the numerous Ag@Au HNRs for the calculated spectra. Therefore, the dipole plasmon coupling of Ag@Au HNRs is essentially relied on the wall thickness, that is, the dosage of $HAuCl_4$ solution in the synthetic process.

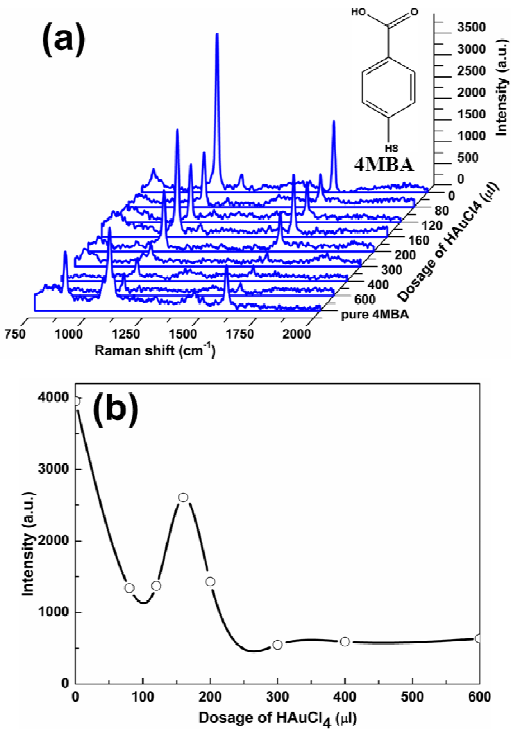

Fig. 6 (a) The SERS spectra of 4MBA-tagged Ag@Au HNRs obtained at different dosages of $HAuCl_4$ solution and the inset is the molecular structural formula of 4MBA, (b) the relationship of the intensity of Raman peak at 1078 cm^{-1} and the dosage of $HAuCl_4$ solution. Sampling conditions of the Raman spectra: the laser power of 49.995 mW and the integration time of 10s.

SERS performance of the Ag@Au HNRs

The SERS performances of Ag@Au HNRs were evaluated by using 4MBA as the Raman reporter molecules. In our experiments, only the electromagnetic contribution originated from the LSPR characteristic of Ag@Au HNRs is responsible to the signal of Raman active molecule 4MBA because the chemical enhancement are minimized under the near-infrared excitation wavelength of 785 nm.[33, 34] Fig. 6(a) gives the SERS spectra of 4MBA linked with the Ag@Au HNRs prepared at the different dosages of $HAuCl_4$ solution. In Fig. 6, the SERS bands of 4MBA display evident fingerprint characteristics, for example, the two dominant Raman peaks at 1078 and 1585 cm^{-1} are ascribed to the ν(C–C) benzene ring-breathing modes,[35] the peaks at 847 cm^{-1} and 1137 cm^{-1} are resulted from the COO– bending mode (δ(COO–)) and the mixed mode (13β(CCC) + ν(C–S) + ν(C–COOH)), respectively, and a stretching mode at 1430 cm^{-1} (ν_s(COO–)).[36, 37] Due to the strong coupling between the transition dipole moment of benzene ring and local electric field in the vicinity of Ag@Au HNRs, the ν(C–C) mode shows a prominent intensity than that of the other modes. Consequently, the intensity of the peak at 1078 cm^{-1} was selected to evaluate the SERS performance of Ag@Au HNRs as shown in Fig. 6(b). It is seen from Fig. 6(b) that the SERS signal of 4MBA-tagged Ag HNPs (corresponding to the zero dosage of $HAuCl_4$ solution) is strongest because the silver supports plasmon resonances with lowest losses throughout most of the visible and near-infrared spectral region and the charge transfer effect between the adsorbed molecule 4MBA and the Ag surface.[38, 39] And the SERS intensity of 4MBA-tagged Ag@Au HNRs prepared at 160 μl of $HAuCl_4$ solution is stronger than that of the other cases. It is possible that the gold shells were happened to collapse in the centre of the two flat [111] planes and exposed the silver nanoparticles from the interior of Ag@Au HNRs, which resulted in the enhancement of SERS signal. As the dosage of $HAuCl_4$ solution continuously increased, the SERS intensities of 4MBA-tagged Ag@Au HNRs exhibit a decreasing trend due to the coating of the gold shell to the silver ring and the increase of the shell thickness.

To present the role of strong electromagnetic enhancements of the Ag@Au HNRs, the local electric field intensity distributions around the Ag HNP and the Ag@Au HNRs were simulated by FEM under irradiating of the monochromatic light at 785 nm. In Fig. 7, as anticipated, the maximum of electric field intensity of Ag HNP is higher than that of Ag@Au HNRs and the areas of strongest local electric field are observed around the corners and edges of these nanostructures due to the accumulation of electric charges in large curvatures of the metal nanostructures.[40] And it is also obvious that the maximums of electric field intensity of Ag@Au HNRs give a trend which firstly decreases and then gently increases as decreasing of the wall thickness, but the case of Ag@Au HNR with a wall thickness of 5.5 nm is an exception. In Fig. 7(b), the strong electric field area was located in the hollow interior of Ag@Au HNR owing to the dominate effect of Ag in the wall. Especially, the Ag@Au HNR with a wall thickness of 5.5 nm exhibited a strongest electric field enhancement. It could be ascribed to the interband contribution with the lowest loss because the imaginary part of the dielectric function of the gold has a minimum value about 660 nm which was approximately agreement with the dipole LSPR peak of the Ag@Au HNR with a wall thickness of 5.5 nm.[38] In addition, the higher electric field intensity shown in Fig. 7(h) demonstrated the contribution of the dipole LSPR peak approached to the excitation wavelength of 785 nm. Comparing Fig. 7 with Fig. 6, it is interesting to find that the SERS behaviours of Ag@Au HNRs corresponding to the different dosages of $HAuCl_4$ solution are significant consistent with the enhancement of electric field of Ag@Au HNRs with different wall thicknesses. Therefore, a reasonable structure of Ag@Au HNR is of great significance for obtaining strong SERS enhancement.

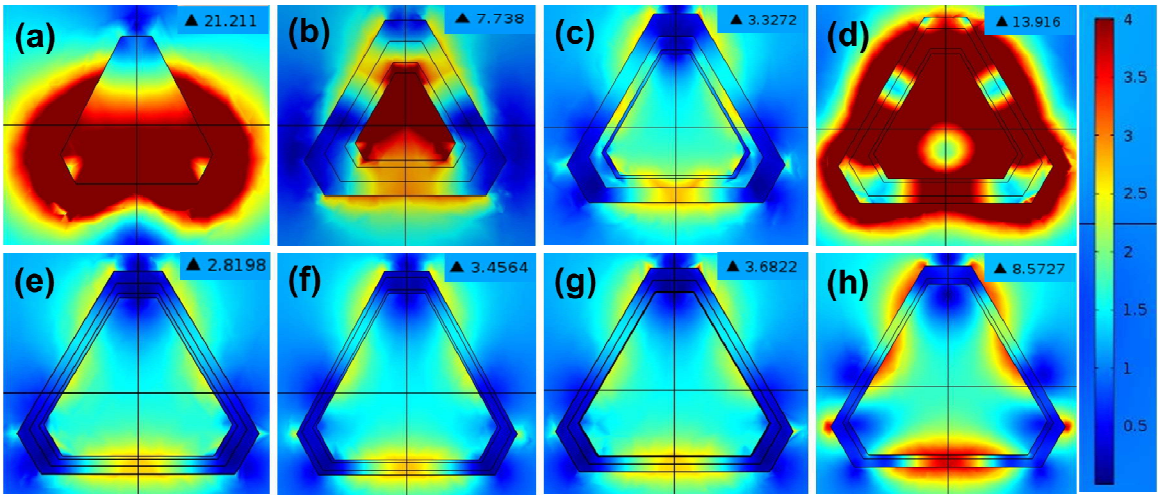

Fig. 7 FEM simulation of the electric field intensity distribution of the (a) Ag HNPs and Ag@Au HNRs with different wall thicknesses: (b) 7 nm, (c) 6 nm, (d) 5.5 nm, (e) 5 nm, (f) 4.5 nm, (g) 4 nm, and (h) 3.5 nm. Here, the permittivity data of gold and silver were obtained from Ref. [38], and the incident plane-wave propagated along vertical direction and polarized along horizontal direction.

For quantifying the SERS enhancement of Ag@Au HNRs prepared with different dosages of $HAuCl_4$ solution, their EF values were calculated by using the following equation:[34]

$$EF = (I_{SERS}/I_{bulk}) \times (N_{bulk}/N_{SERS}) \quad (2)$$

where I_{SERS} and I_{bulk} are the integrated intensities of the same Raman band in the SERS and bulk Raman spectra, respectively; N_{bulk} is the number of molecules probed in the pure 4MBA solution; and N_{SERS} is the number of 4MBA molecules adsorbed on the surfaces of Ag@Au HNRs. In Fig. 6, the intensities of SERS peaks at 1078 cm^{-1} were selected to calculate the EF values of Ag@Au HNRs. As an example, Fig. 8 provides the SERS spectrum of 4MBA-taaged Ag@Au HNRs obtained at 160 µl of $HAuCl_4$ solution and the Raman spectrum of 4MBA solution with the concentration of 10 mM. Thus, I_{SERS} and I_{bulk} are integrated to be 7.9×10^4 and 9.31×10^4, respectively. In our experimental conditions, the diameter of illumination focus of the Raman spectrometer was 2.39 µm for the 20× objective lens with N.A. = 0.4, and the penetration depths of laser beam at 785 nm are 1.02 µm and 0.86 µm for the 4MBA solution and the 4MBA-tagged Ag@Au HNRs solution, respectively. Then, the N_{bulk} and N_{SERS} corresponding to the illuminated volumes of 4.51 μm^3 and 3.83 μm^3 were calculated to be 1.1×10^{11} and 1.7281×10^4, respectively. So, the enhancement factor of the Ag@Au HNRs $EF_{160\mu l} = 4.99\times10^6$. Similarly, for the other Ag@Au HNRs prepared at different dosages of $HAuCl_4$ solution, their EF values can be given as $EF_{0\mu l} = 6.81\times10^6$, $EF_{80\mu l} = 2.81\times10^6$, $EF_{120\mu l} = 2.37\times10^6$, $EF_{200\mu l} = 3.63\times10^6$, $EF_{300\mu l} = 2.39\times10^6$, $EF_{400\mu l} = 2.59\times10^6$, and $EF_{600\mu l} = 2.72\times10^6$, respectively. Therefore, it demonstrates that the as-synthesized Ag@Au HNRs exhibit superior SERS performances and can be used as an excellent SERS probes for the application in biosensing field.

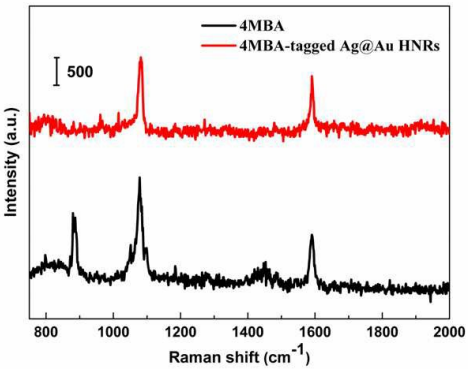

Fig. 8 The Raman spectrum of 4MBA solution and the SERS spectrum of 4MBA-tagged Ag@Au HNRs prepared at 160 µl $HAuCl_4$ solution.

Conclusions

In this work, the Ag@Au HNRs were synthesized by a facile galvanic replacement route with the help of the Ag HNPs as structure-directing templates, and their morphologies and sizes can be tuned by altering the added dosage of $HAuCl_4$ solution. The Ag@Au HNRs synthesized at different dosages of $HAuCl_4$ solution exhibited the strong structure-dependent LSPR characteristics such as the remarkable red-shifts of dipole LSPR peaks. Interestingly, both the experimental and calculated results show that the positions of the LSPR peaks of the Ag@Au HNRs corresponding to the dosages of $HAuCl_4$ solution displayed a modified Lorentz curve. In addition, the as-synthesized Ag@Au HNRs exhibit superior SERS performance owing to the strong electromagnetic enhancement resulting from the plasmon hybridization of the silver ring and the gold shell. It is expected that the Ag@Au HNRs have promising applications related to SERS sensors.

Acknowledgements

This work was supported by the National Natural Science Foundation of China (Grant nos. 112064038, 61275153, and 61320206014), the European Regional Development Fund-FESR of POR Campania 2007-2013 - Call Innovation Window (Project title: Kit for Brucella Abortus e B. Melitensis nano-BIosensing Rapid detection- AMBRA), and the K. C. Wong Magna Foundation of Ningbo University, China.

Notes and references

[a] *Institute of Photonics, Faculty of Science, Ningbo University, Ningbo 315211, China. Tel: +86-574-87600794; Fax: +86-574-87600744; E-mail: zhoujun@nbu.edu.cn*
[b] *School of Information Science and Engineering, Xinjiang University, Urumqi 830046, China.*
[c] *Institute of Cybernetics "E. Caianiello" of CNR, Via Campi Flegrei 34, 80072 Pozzuoli, Ital.*

† Electronic Supplementary Information (ESI) available: Size effect of the gold nanosphere, relationship of wall thickness and the dosage of $HAuCl_4$ solution, and plasmon hybridization.

1 Y. Yin and D. Talapin, *Chem. Soc. Rev.*, 2013, **42,** 2484-2487.
2 M. Vollmer and U. Kreibig, *Springer Ser. Mat. Sci.*, 1995, **25**.
3 L. Polavarapu and L. M. Liz-Marzán, *Phys. Chem. Chem. Phys.*, 2013, **15**, 5288-5300.
4 Y. Sun, B. Mayers and Y. Xia, *Adv. Mater.*, 2003, **15**, 641-646.
5 A. Agarwal, S. W. Huang, M. O'Donnell, K. C. Day, M. Day, N. Kotov and S. Ashkenazi, *J. Appl. Phys.*, 2007, **102**, 064701.
6 D. Lee and S. Yong, *J. Phys. Chem. C*, 2015, **119**, 7873-7882.
7 T. Jiang, L. Zhang and J. Zhou, *Analyst*, 2014, **139**, 5894-5901.
8 J. M. McLellan, A. Siekkinen, J. Chen and Y. Xia, *Chem. Phys. Lett.*, 2006, **427**, 122-126.
9 M. Xue and Y. Tan, *Nanoscale*, 2014, **6**, 12500-12514.
10 G. S. Métraux, Y. C. Cao, R. Jin and C. A. Mirkin, *Nano Lett.*, 2003, **3**, 519-522.
11 G. Fu, L. Ding, Y. Chen, J. Lin, Y. Tang and T. Lu, *CrystEngComm*, 2014, **16**, 1606-1610.
12 L. Chen, J. M. Chabu and Y. Liu, *RSC Adv.*, 2013, **3**, 4391-4399.
13 J. Gao, X. Ren, D. Chen, F. Tang and J. Ren, *Scripta Mater.*, 2007, **57**, 687-690.
14 Y. Wang, H. Chen, S. Dong and E. Wang, *J. Chem. Phys.*, 2006, **125**, 044710.
15 K. An and T. Hyeon, *Nano Today*, 2009, **4**, 359-373.
16 M. Chen and L. Gao, *Inorg. Chem.*, 2006, **45**, 5145-5149.
17 E. Gonzalez, J. Arbiol and E. F. Puntes, *Science*, 2011, **334**, 1377-1380.

18 L. Wang and Y. Yamauchi, *J. Am. Chem. Soc.*, 2013, **135**, 16762-16765.
19 Y. Li, P. Zhou, Z. Dai, Z. Hu, P. Sun and J. Bao, *New J. Chem.*, 2006, **30**, 832-837.
20 J. M. Li, Y. Yang and D. Qin, *J. Mater. Chem.C*, 2014, **2**, 9934-9940.
21 S. Chen and D. L. Carroll, *Nano Lett.*, 2002, **2**, 1003-1007.
22 N. Ortiz and S. E. Skrabalak, *Cryst. Growth Des.*, 2011, **11**, 3545-3550.
23 Y. Sun and Y. Xia, *Anal. Chem.*, 2002, **74**, 5297-5305.
24 A. I. Kirkland, D. A. Jefferson, D. G. Duff, P. P. Edwards, I. Gameson, B. F. G. Johnson and D. J. Smith, *Proc. R. Soc. London A*, 1993, **440**, 589-609.
25 Y. Yin, R. M. Rioux, C. K. Erdonmez, S. Hughes, G. A. Somorjai and A. P. Alivisatos, *Science*, 2004, **304**, 711-714.
26 Y. Liu, J. Zhou, B. Wang, T. Jiang, H. P. Ho, L. Petti and P. Mormile, *Phys. Chem. Chem. Phys.*, 2015, **17**, 6819-6826.
27 Y. Aray, J. Rodriguez and D. Vega, *J. Phys. Chem. B*, 2000, **104**, 4608-4612.
28 M. R. Langille, M. L. Personick and C. A. Mirkin, *Angew. Chem. Int. Ed.*, 2013, **52**, 13910-13940.
29 R. Contreras-Cáceres, A. Sánchez-Iglesias, M. Karg, I. Pastoriza-Santos, J. Pérez-Juste, J. Pacifico, T. Hellweg, A. Fernández-Barbero and L. M. Liz-Márzan, *Adv. Mater.*, 2008, **20**, 1666-1670.
30 S. A. Clough and F. X. Kneizys, *Appl. Optics*, 1979, 18, 2329-2333.
31 P. Mulvaney, *Langmuir*, 1996, **12**, 788-800.
32 N. J. Halas, S. Lal, W. S. Chang, S. Link and P. Nordlander, *Chem. Rev.*, 2011, **111**, 3913-3961.
33 R. A. Álvarez-Puebla, *J. Phys. Chem. Lett.*, 2012, **3**, 857-866.
34 Q. Zhang, N. Large and H. Wang, *ACS Appl. Mater. Interfaces*, 2014, **6**, 17255-17267.
35 S. W. Bishnoi, C. J. Rozell, C. S. Levin, M. K. Gheith, B. R. Johnson, D. H. Smith and N. J. Halas, *Nano Lett.*, 2006, **6**, 1687-1692.
36 A. Michota and J. Bukowska, *J. Raman Spectrosc.*, 2003, **34**, 21-25.
37 Y. He, S. Su, T. T. Xu, Y. L. Zhong, J. A. Zapien, J. Li, C. H. Fan and S. T. Lee, *Nano Today*, 2011, **6**, 122-130.
38 P. B. Johnson and R. W. Christy, *Phys. Rev. B*, 1972, **6**, 4370-4379.
39 F. J. Adrian, *J. Chem. Phys.*, 1982, **77**, 5302-5314.
40 Z. Y. Li and Y. Xia, *Nano Lett.*, 2009, **10**, 243-249.
41 J. A. Scholl, A. L. Koh and J. A. Dionne, *Nature*, 2012, **483**, 421-428.

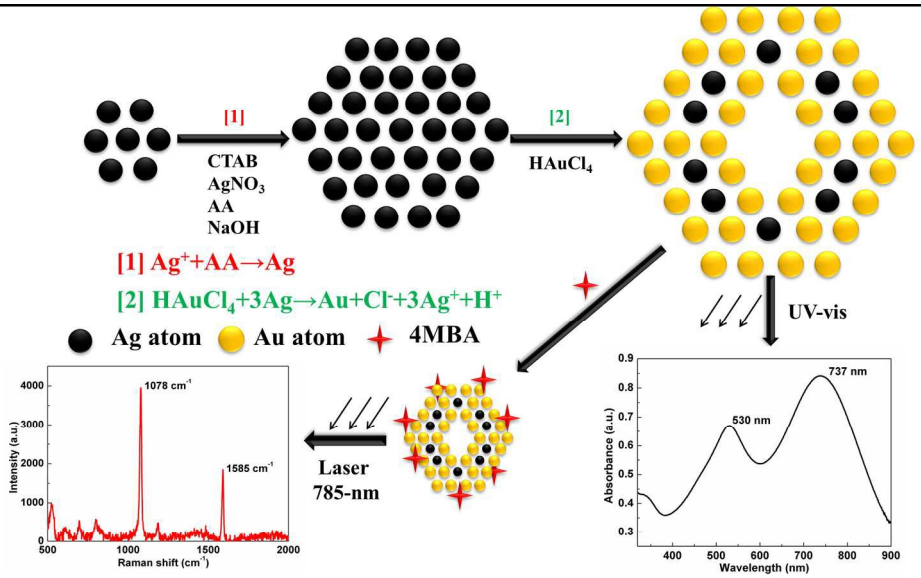

Ag@Au hexagonal nanorings synthesized through a one-spot galvanic replacement route and its distinctive LSPR characteristic and SERS performance.

340x215mm (150 x 150 DPI)